Eur. Phys. J. D **26**, 83–90 (2003)
DOI: 10.1140/epjd/e2003-00075-y

THE EUROPEAN PHYSICAL JOURNAL D

ATI of complex systems: Ar and C_{60}

E. Cormier[1,a], P.-A. Hervieux[2], R. Wiehle[3], B. Witzel[3], and H. Helm[3]

[1] Centre Lasers Intenses et Applications[b], Université Bordeaux I, 351 cours de la Libération, 33405 Talence, France
[2] LPMC, Institut de Physique, Technopôle 2000, 57078 Metz, France
[3] Fakultät für Physik, Albert-Ludwigs-Universität, Stefan-Meier-Strasse 19, 79104 Freiburg, Germany

Received 21 November 2002 / Received in final form 20 December 2002
Published online 24 April 2003 –

Abstract. Above threshold ionization of two structurally different systems is presented namely a rare gas such as argon and the more complex C_{60} fullerene. We show that the ionization dynamics is different and is dominated by the presence of high-lying Rydberg states in Ar and low-lying bound states in C_{60}. The study is based on a theoretical (solving the time dependent Schrödinger equation) and/or experimental (using measurements from a photoelectron imaging spectrometer) aspect.

PACS. 33.80.Rv Multiphoton ionization and excitation to highly excited states (e.g., Rydberg states) – 32.80.Fb Photoionization of atoms and ions – 36.40.-c Atomic and molecular clusters – 33.60.-q Photoelectron spectra – 61.48.+c Fullerenes and fullerene-related materials

1 Introduction

Strong field laser-atom interactions such as multiphoton ionization (MPI) or above threshold ionization (ATI) [1] in gaseous medium have been investigated for more than two decades with infrared light [2,3] as well as with short wavelengths [4–6]. The study of ATI has been recently extended to measurements connected to multiple ionization [7,8]. However, most of the works have been carried out in rare gases where the field-induced mechanisms are now well understood. It is only recently that this field has gained a new interest after ATI had been observed in complex systems such as C_{60} clusters [9]. We first present a review of the processes involved in such an interaction through a detailed comparison between experiment and theory in the case of Ar. The simulation has been designed to include all the experimental parameters and is able to reproduce all the measurements quantitatively. The key point of this validated model is that it allows to recover in great detail all the underlying mechanisms. We then discuss the ionization processes when associated with ATI of C_{60} by analyzing the results provided by the simulations. This approach allows a detailed description of the ionization dynamics for ultrashort pulse duration (<30 fs) and the role of the cluster structure which can then be compared to the situation observed with rare gases.

[a] e-mail: Eric.Cormier@celia.u-bordeaux.fr
[b] UMR 5107 du CNRS

2 Argon

2.1 PEIS measurements

During the interaction of the laser beam and the gaseous medium, electrons are freed by ionization mechanisms. The experiment is designed to record the electron angular and energy distribution at the same time, using a photoelectron imaging spectrometer (PEIS) [10]. A linearly polarized Ti:sapphire laser beam ($\tau = 100$ fs, $E_{\max} = 1$ mJ) is focussed into a vacuum chamber containing argon gas at pressures varying between 10^{-7} and 10^{-4} mbar. The wavelength is centered at 800 nm with a full width at half maximum of 9 nm. A constant electric field of 100 V/cm allows the projection of the photoelectrons onto a two-dimensional detector consisting of a pair of multichannel plates and a phosphor screen. Their impact positions are recorded with a computer based CCD (charge-coupled device) camera. The software in combination with the high repetition rate of the laser of 1 kHz allows the accumulation of 10^5–10^7 single electron signals per image. Electrons created with the same kinetic energy appear inside a well defined circular pattern. The radius is proportional to the momentum of the electron distribution hitting the detector. Each image contains the signal of photoelectrons created by different processes resulting in different electron energies and is therefore a superposition of many corresponding patterns. Because the photoelectron distribution is symmetric with respect to the polarization axis of the laser, an inverse Abelian transformation can be used to convert the images into angle-resolved momentum

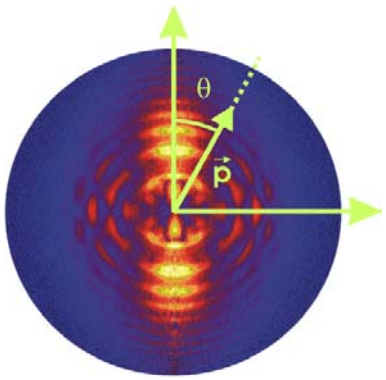

Fig. 1. Example of a PEIS image. The radial distance is proportional to the electron momentum. The emission angle with respect to the laser polarization is given by θ.

distributions [11]. The center of the transformed images correspond to zero momentum. The distance from the center to a particular point is proportional to the electrons momentum.

2.2 PEIS simulations

The theoretical results presented in Section 2.3 are issued from a complete simulation of the experiment accounting for first, the interaction of Ar with the laser pulse on the atomic scale, second, the macroscopic extension of the interaction volume delimited by the intersection of the laser beam and the gas leak and third, the electron detection procedure (PEIS) as described in the previous section.

Ionization due to a single atom is computed by numerically solving the associated time dependent Schrödinger equation (TDSE) in the single active electron (SAE) approximation:

$$\mathrm{i}\frac{\partial}{\partial t}\Psi(\mathbf{r},t) = \left[-\frac{1}{2}\nabla^2 + V(\mathbf{r}) - \mathbf{A}(t)\cdot\mathbf{p}\right]\Psi(\mathbf{r},t). \quad (1)$$

The implementation of the procedure used to solve equation (1) has been already reported in [12] and more recently in [13]. The rather complex attractive atomic potential due to the nucleus screened by the inner shell electrons is accounted for through the central potential $V(\mathbf{r}) = V(r)$. A recently published model-potential [14] for argon provides a very accurate description of both the atomic structure (bound states) of the bare atom and the rescattering properties of the ion core. These two features are essential in the present case since ATI is mainly dominated by intermediate resonances due to high lying Rydberg states for the low energy photoelectrons and by backscattering on the parent ion core for high energy photoelectrons.

The electron angular and momentum distribution is computed at the end of the pulse by projecting the total final wave-function onto eigen-states corresponding to electrons emitted in the parent ion continuum with a given momentum vector:

$$\frac{\partial P}{\partial E_k \partial\theta_k} = |\langle f_{\mathbf{k}}^- | \Psi(t_{\mathrm{end}})\rangle|^2 \quad (2)$$

where $|f_{\mathbf{k}}^-\rangle$ is the Coulomb wave-function corresponding to an outgoing electron with momentum $\mathbf{k}$, which reads in terms of partial waves:

$$f_{\mathbf{k}}^-(\mathbf{r}) = \sum_{l=0}^{l_{\max}} (\mathrm{i})^l \mathrm{e}^{-\mathrm{i}\delta_l} \Phi_{E_k}^l(\mathbf{r}) Y_l^{0^*}(\theta_k, 0) \quad (3)$$

where δ_l is the Coulombic phase and where $\Phi_{E_k}^l(\mathbf{r})$ is a discretized continuum wavefunction.

The procedure described above provides the probability of observing an electron emitted with a particular energy and direction during ionization of a single atom by the laser field with a given peak intensity. Unfortunately the experiment collects electrons originating from atoms located anywhere in the interaction volume and therefore experiencing different peak intensities and field phase across the beam profile. This latter fact prevents us from directly comparing the experimental data with the theoretical electron spectra. As a matter of fact, except for low intensity spectra, the ATI peaks never appear at the expected energy location. A one to one correspondence between theoretical and experimental spectra at given energies is never possible. Moreover, ATI substructures raise or disappear independently in both data. Actually, trying to interpret the measurement on the view of the theoretical results can be misleading. It is therefore a necessity to compute electron spectra resulting from the interaction of the laser beam with all the atoms contained in the interaction volume. This is achieved by computing the yield of electrons emitted in the θ_k direction with a kinetic energy E_k as [3,15]:

$$N(E_k,\theta_k) = \rho \int \frac{\partial P(I)}{\partial E_k \partial\theta_k}\frac{\partial V}{\partial I}\mathrm{d}I \quad (4)$$

where ρ is the density of atoms in the gas target (assumed constant). The volume $(\partial V/\partial I)\mathrm{d}I$ experiencing an intensity between I and $I+\mathrm{d}I$ is defined in [16] for a Lorentzian (propagation direction) and Gaussian (transverse direction) beam profile. In practice, less than a hundred partial spectra $\partial P/\partial E_k\partial\theta_k$ corresponding to various intensities are computed. We then interpolate those spectra with respect to I before performing the summation (4).

The multi-intensity photoelectron spectra are used as an input for a simulation of the experiment. Random photoelectron energies and emission angles were generated. The probability was given by the calculated multi-intensity spectra. Experimental parameters are used to calculate the impact position of the detector. The single electron response of each simulated electron was taken into account by choosing one out of 1000 experimentally determined single event signals. The technique allows us to include the experimental reduction of the resolution due to the limited number of the pixel of our CCD-device as well as the statistical distribution of the signal produced

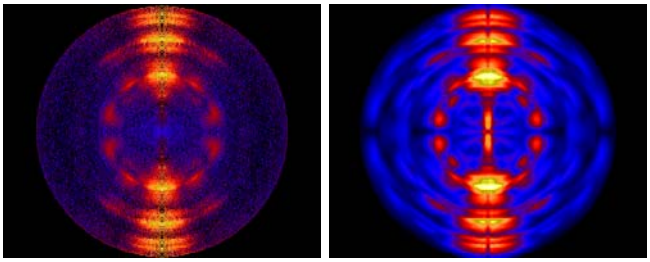

Fig. 2. Angular and momentum distribution of ATI of Ar for $I = 3.8 \times 10^{13}$ W/cm^2. Experiment: left, theory: right.

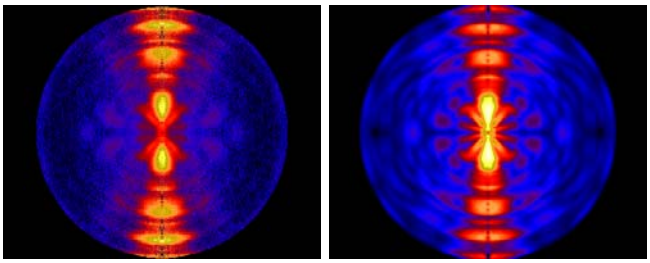

Fig. 3. Angular and momentum distribution of ATI of Ar for $I = 5 \times 10^{13}$ W/cm^2. Experiment: left, theory: right.

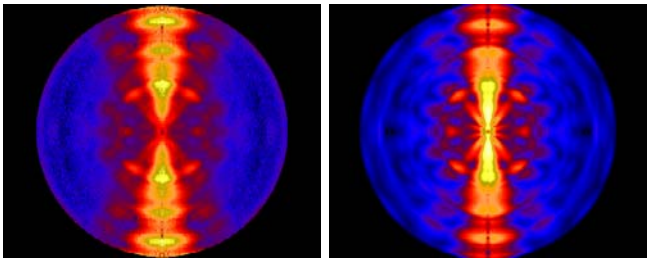

Fig. 4. Angular and momentum distribution of ATI of Ar for $I = 7 \times 10^{13}$ W/cm^2. Experiment: left, theory: right.

by one single electron, when it hits the detector. A calculation is the averaged signal from 10^6 electrons and were extracted in the same way as the experimental ones.

2.3 Discussion

2.3.1 Comparing theory and experiment

In this section, we first comment the excellent matching between the experiment and our sophisticated model and how this great asset is emphasized in the process of identifying all the underlying dynamical mechanisms involved.

We present in Figures 2, 3 and 4 a selection of 3 PEIS images that we consider representative of the various regimes encountered. As can be seen, even if the images show drastic changes as the intensity is raised, the comparison is very good. It is even more impressive if one looks at the same data however presented in more conventional graphics such as the electron spectrum and the angular distribution of given ATI peaks as shown in Figure 5. The first column represents the electron energy distribution for the 3 selected laser peak intensities. These are obtained by integrating over angles the PEIS data from $-10°$ to $10°$. The agreement is very good: both the simulated and measured data exhibits peaks at the same position with the same amplitude for all intensities. Moreover, the angular distributions are very well reproduced for all the peaks.

2.3.2 Channel switching

As can be seen on the PEIS plots (Figs. 2–4), drastic changes are observed in the way electrons are ejected from their parent ion as the laser intensity is raised. At low intensity, it requires 11 photons to ionize Ar. When the laser strength is increased, the electrons acquire a significant ponderomotive energy (proportional to the field intensity) due to their oscillatory motion in the field. Thus, to achieve ionization, more energy should be deposited in the system. Indeed, for intensities above $I = 2 \times 10^{13}$ W/cm^2 12 photons are necessary to bring the system into the continuum. This particular intensity is referred to as the 11-photon ionization channel switching intensity [17]. The successive channels close, in theory, at $I = 4.6 \times 10^{13}$ W/cm^2, $I = 7.2 \times 10^{13}$ W/cm^2, $I = 9.8 \times 10^{13}$ W/cm^2 for the 12-, 13- and 14-photon ionization respectively. Short after a channel has switched, the ionization is dominated by resonant multiphoton ionization with the high lying Rydberg states [18,19]. Due to the dipole selection rules, resonant states have different parity in two successive channels inducing different dynamics. We therefore have chosen to present and discuss PEIS plots corresponding to ionization in the 12-photon ionization channel (Fig. 2), at the channel switching (Fig. 3) and in the 13-photon ionization channel (Fig. 4). Note that the present discussions hold for higher channel switchings.

2.3.3 Resonant ionization: Rydberg states identification procedure

Apart from ionizing the system, the field also induces a distortion and AC Stark shifts the atomic levels. Accordingly, the ionization potential is increased by the ponderomotive energy $U_p = I/4\omega^2$. Because the field has a temporal shape, the modification of the atomic structure dynamically induces resonances which boost the ionization when the detuning vanishes. Note that the resonance can take place before or after the laser pulse maximum. For a given peak intensity, an electron detected with a particular kinetic energy may have been emitted long before the field maximum. Alternatively, since the beam has a spatial dependence, this electron may come from a location in the interaction volume which is off the propagation axis and therefore originating from an atom experiencing a lower temporal peak intensity.

These contributions might dominate the spectrum since the ionization enhancement due to a particular resonance (which happen for an atom experiencing a fixed intensity) always produces electrons at the same energy. No matter where or when they have been emitted,

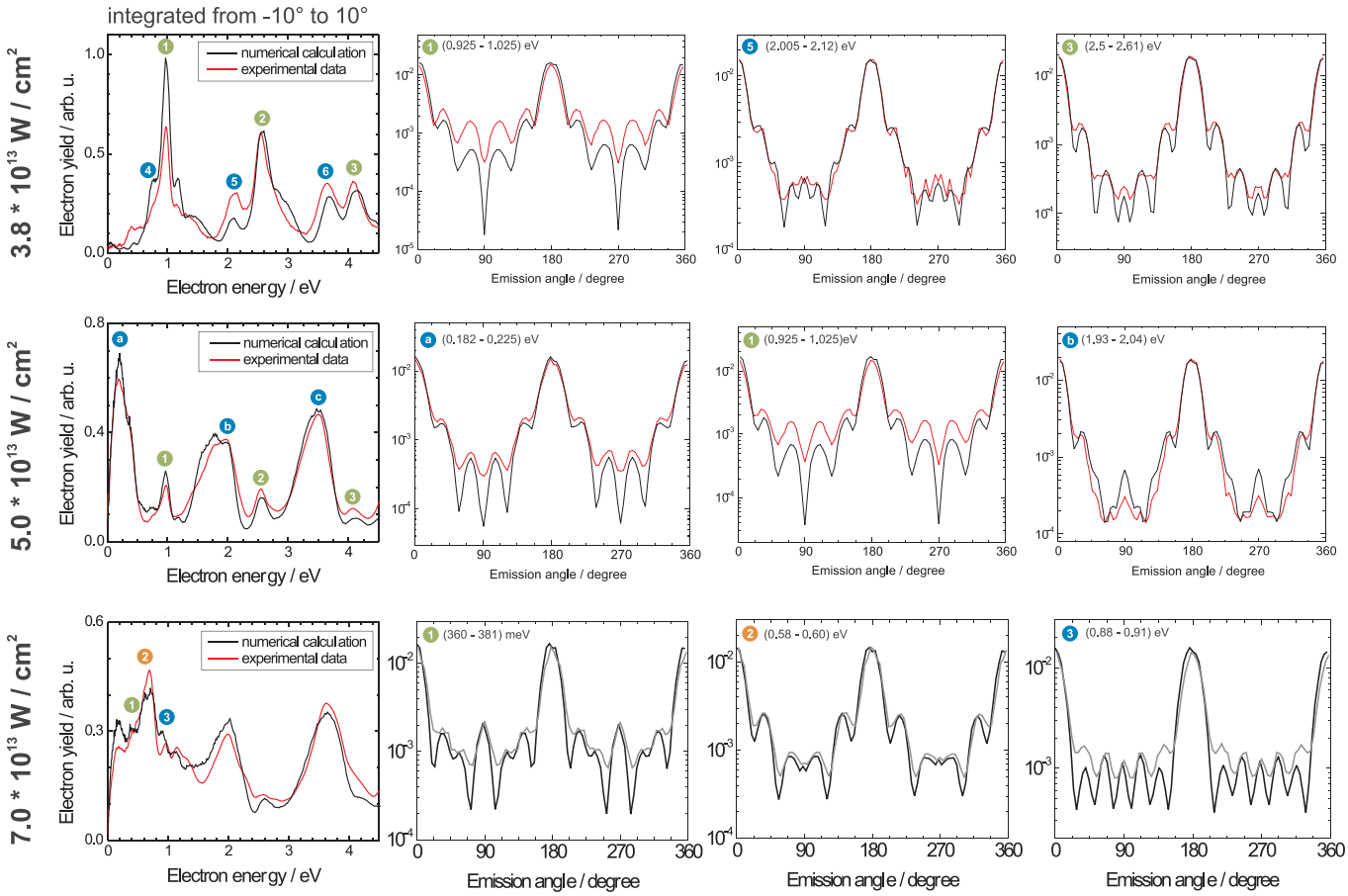

Fig. 5. Angular distribution of several selected ATI peaks of Ar. Note the logarithmic scale on the angular distributions.

the contributions add up at the same energy in the spectrum thus giving peaked structures.

The procedure to identify, in an univocal manner, the resonances is based on the close analysis of both the experimental and the theoretical results. This procedure is illustrated in the case of the first peak labelled (1) in the upper left graph in Figure 5 but has been applied to all the peaks.

The electrons corresponding to that peak are emitted with a kinetic energy $E_k = 1$ eV. The calculation says that, although the peak intensity in that case is $I = 3.8{\times}10^{13}$ W/cm^2, these electrons are emitted by atoms experiencing a resonant intensity of $I_\mathrm{r} = 3.2 \times 10^{13}$ W/cm^2 as shown in Figure 6. that is atoms located somewhere around the focus. The partial wave decomposition at $I_\mathrm{r} = 3.2 \times 10^{13}$ W/cm^2 and for electrons of 1 eV gives the following statistics:

	$l=1$	$l=3$	$l=5$	$l=7$
P	8%	7%	66.5%	17.5%

The theory predicts a dominant angular momentum of $l = 5$ which is confirmed by the experiment as in the second upper graph of Figure 5 where 5 minima clearly appear between 0 and 180°. These electrons are produced by one photon absorption from one of the Rydberg states having shifted into resonance. The symmetry of this resonance is therefore either $l = 4$ or $l = 6$. If we now assume that the high-lying Rydberg states ponderomotively shift as the ionization potential (*i.e.* by U_p) the resonant level should lie around $E = -0.02065$ a.u. The nearest candidate is the $5g$ state ($E_{5g} = -0.02$ a.u. and there are no

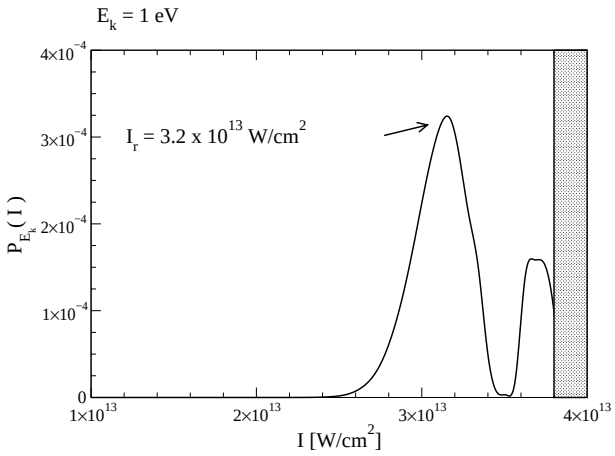

Fig. 6. Intensity dependence of the electron yield with $E_k = 1$ eV for a peak intensity of $I = 3.8 \times 10^{13}$ W/cm^2. The main contribution is from atoms experiencing a resonant intensity of $I_\mathrm{r} = 3.2 \times 10^{13}$ W/cm^2.

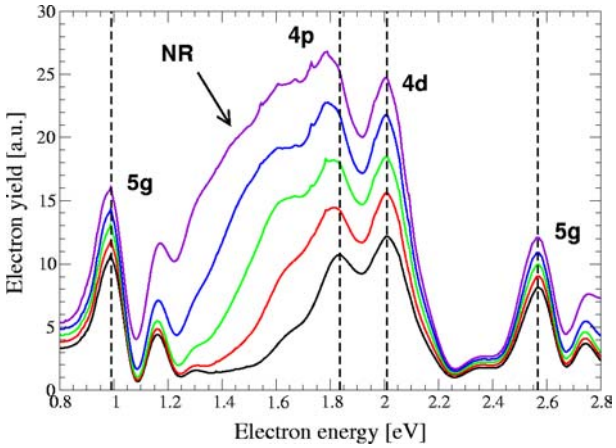

Fig. 7. High resolution simulated electron distribution at $\theta = 0°$ as a function of intensity. The central peak correspond to peak (b) in Figure 5. The intensities range from $I = 4.6 \times 10^{13}$ W/cm^2 up to $I = 5.4 \times 10^{13}$ W/cm^2. Note the non-resonant ionization located between 1.3 and 1.7 eV shifting downward with increasing intensity. Note also the double structure splitting for higher field strength.

states nearby in the $l = 6$ symmetry) which, in theory, shifts into resonance with the absorption of 11 photons at an intensity of $I = 2.9 \times 10^{13}$ W/cm^2. The discrepancy between this intensity and I_r is due to the fact that the resonant process should last for a while for the production of electrons to be significant. Therefore, we expect that the observed resonance intensity is higher than the theoretical one so that resonant ionization last several femtoseconds around the field peak intensity.

2.3.4 AC Stark splitting

The above mentioned procedure is robust and has been applied to almost all peaks. However in cases where other mechanisms come into play, the identification is not straightforward. At $I = 5 \times 10^{13}$ W/cm^2, the peak located around $E_k = 2$ eV is broad and the experimental resolution is not sufficient to conclude on the origin of the broadening. This problem have been circumvented by going back to the theoretical calculations before simulating the detection procedure which degrades the resolution. High resolution spectra of that peak are shown in Figure 7 for various peak intensities. The graph clearly reveals 2 sharp resonances (1.81 eV and 2 eV) and a broad structure which is explain in the next section. The higher resonance (at 2 eV) is safely attributed to (11+2)-photon ATI through the $4d$ state. However, there is no state to trivially assign to the lower resonance. The energy levels of argon are such that the $4d$ is almost resonantly coupled with the inner $4p$ state by a photon of 1.55 eV. Since the applied field is very strong, the coupling will repeal these two states and lead to a splitting of the ionization peak. The structure at 1.81 eV is therefore due to the $4p$ and the double structure results from the dressed transition $4p - 4d$. The evidence for that is, unlike isolated resonances, that the peak attributed to $4p$ shifts downward as the intensity is increased giving rise to the AC-Stark splitting.

2.3.5 Non-resonant ionization

The broadening observed in the the peak around 1.8 eV in Figure 7 is not only due to the splitting but also to non-resonant ionization. Unlike resonant ionization where the contributions always add up at the same electron energy, non-resonant peaks increase very rapidly (mainly like I^N where N is the minimum number of photons absorbed to reach this energy) and shift downward by the ponderomotive energy U_p as the intensity is raised. This situation happens over intensity ranges where no Rydberg states come into resonance [20]. We have observed it only in the high resolution spectra of Ar but it happens to be more visible in ATI of Xe [21].

2.4 Conclusion

We have presented data recorded with photoelectron imaging spectrometer (PEIS). These data have been successfully reproduced in great details through a complete theoretical calculation of the experiment including: (1) the single atom response (non-perturbative theory), (2) the integration over the interaction volume and (3) the simulation of the detection procedure. The merging of the informations coming from both the experimental and the calculations allows a robust identification of the many processes involved (channel switching, resonant ionization, ...) in the ATI of Ar. The availability of a higher resolution in the theoretical data has revealed non-resonant ionization as well as AC Stark splitting.

3 C_{60}

3.1 Electronic structure

The electronic ground-state of the molecule C_{60} is obtained by using a modified version of the spherical jellium model of Puska and Nieminen [22]. In our model, a rigid shell with smooth surfaces having a constant positive charge distribution ρ_0 is introduced

$$\rho_+(\mathbf{r}) = \frac{\rho_0}{1 + \exp\left\{\left[|r - R| - \Delta R\right]/d\right\}} \tag{5}$$

where $R = 6.7$ a.u. and $d = 0.2$ a.u. are, respectively, the radius of C_{60} and a surface parameter. The thickness of the shell, ΔR, is determined by requiring charge neutrality with a given number of valence electrons. The background density, ρ_0, (or the corresponding density parameter $r_s = (4\pi\rho_0/3)^{-1/3}$) is an adjustable parameter. As in reference [22], we have used $r_s = 1.2$ a.u., which leads to $\Delta R = 1.57$ a.u. The presence of the carbon ion

cores within the rigid shell is simulated by using a pseudopotential

$$V_{\rm ps}(r) = \frac{-V_0}{1+\exp\left\{\left[|r-R|-\Delta R\right]/d\right\}}. \quad (6)$$

The depth of the potential well, V_0 is another adjustable parameters of the model.

In the Kohn-Sham formulation of density functional theory, the ground-state electronic density $\rho_{\rm C}$ of an N-electron system is written in terms of single-particle orbitals ϕ_i

$$\rho_{\rm C}(\mathbf{r}) = \sum_{i=1}^{N} \rho_i(\mathbf{r}) = \sum_i |\phi_i(\mathbf{r})|^2 \ . \quad (7)$$

These orbitals obey the Schrödinger equation

$$\left[-\frac{1}{2}\nabla^2 + V_{\rm eff}(\mathbf{r})\right]\phi_i(\mathbf{r}) = \epsilon_i\phi_i(\mathbf{r}) \ , \quad (8)$$

where $V_{\rm eff}(\mathbf{r})$ is an effective single-particle potential given by

$$V_{\rm eff}(\mathbf{r}) = V_{\rm jel}(r) + V_{\rm H}(\rho_{\rm C}(\mathbf{r})) + V_{\rm xc}(\rho_{\rm C}(\mathbf{r})) \ , \quad (9)$$

where $V_{\rm H}(\rho_{\rm C}(\mathbf{r}))$ is the Hartree potential

$$V_{\rm H}(\rho_{\rm C}(\mathbf{r})) = \int \frac{\rho_{\rm C}(\mathbf{r}')}{|\mathbf{r}-\mathbf{r}'|}\,{\rm d}\mathbf{r}' \quad (10)$$

and

$$V_{\rm jel}(r) = -\int \frac{\rho_+(\mathbf{r}')}{|\mathbf{r}-\mathbf{r}'|}\,{\rm d}\mathbf{r}' + V_{\rm ps}(r) \ . \quad (11)$$

$V_{\rm xc}(\rho_{\rm C}(\mathbf{r}))$ is the exchange-correlation potential. Since the form of $V_{\rm xc}$ is not known in general, several approximations have been proposed in the literature. In this work, we have used the form obtained by Gunnarsson and Lundqvist [23] in the framework of the local-density approximation (LDA)

$$V_{\rm xc}(\rho_{\rm C}(\mathbf{r})) = -\left(\frac{3\rho_{\rm C}(\mathbf{r})}{\pi}\right)^{1/3} - 0.0333\,\log\left(1+\frac{11.4}{r_{\rm s}(\mathbf{r})}\right) \quad (12)$$

where $r_{\rm s}(\mathbf{r}) = [3/4\pi\rho_{\rm C}(\mathbf{r})]^{1/3}$ is the local Wigner-Seitz radius. To correct for the unphysical asymptotic behavior of the exchange term in the LDA, we have introduced the self-interaction correction (SIC) of Perdew and Zunger [24]. The SIC restores the correct $-1/r$ asymptotic behavior of the effective potential at large distances, which is essential to properly describe the ionization process. Note also that without this correction the bound state energies are lowered leading to wrong ionization potentials [25].

We have chosen a value of $V_0 = 0.68$ a.u. in equation (6) in order that the energy of the highest occupied orbital (HOMO) is close to the experimental ionization potential of C_{60} (7.54 ± 0.04 eV [26]). This value is significantly different from that used by Puska and Nieminen because the latter authors did not not include the SIC term. As in reference [22], we have chosen for our representation a system of 250 electrons instead of 240 valence electrons that actually correspond to C_{60}. The reason is that, in the spherical representation, 240 electrons do not lead to a closed-shell system as in the real C_{60} molecule (see [22] for details).

Table 1. Energy levels of the occupied and the first unoccupied orbitals of C_{60} measured from the first ionization threshold. l is the angular momentum and n the principal quantum number. n_e refers to the number of electrons occupying the orbital.

	Occupied			Unoccupied		
n_e	(l,n)	E (a.u.)	E (eV)	(l,n)	E (a.u.)	E (eV)
2	$(0,1)$	-1.23926	-33.718	$(5,2)$	-0.25366	-6.902
6	$(1,1)$	-1.21533	-33.067	$(0,3)$	-0.17822	-4.849
10	$(2,1)$	-1.16798	-31.779	$(1,3)$	-0.13130	-3.573
14	$(3,1)$	-1.09807	-29.877	$(6,2)$	-0.12230	-3.328
18	$(4,1)$	-1.00677	-27.392	$(2,3)$	-0.08925	-2.429
22	$(5,1)$	-0.89538	-24.361	$(10,1)$	-0.08569	-2.332
26	$(6,1)$	-0.76529	-20.822	$(0,4)$	-0.06699	-1.823
2	$(0,2)$	-0.62806	-17.088	$(3,3)$	-0.05318	-1.447
30	$(7,1)$	-0.61789	-16.811	$(1,4)$	-0.04386	-1.194
6	$(1,2)$	-0.59988	-16.321	$(0,5)$	-0.03288	-0.895
10	$(2,2)$	-0.54596	-16.321	$(0,5)$	-0.03288	-0.895
10	$(2,2)$	-0.54596	-14.854	$(2,4)$	-0.03179	-0.865
14	$(3,2)$	-0.46869	-12.752	$(1,5)$	-0.02528	-0.688
34	$(8,1)$	-0.45458	-12.367	$(4,3)$	-0.02469	-0.672
18	$(4,2)$	-0.37036	-10.078	$(3,4)$	-0.02360	-0.642
38	$(9,1)$	-0.27673	-7.528	$(0,6)$	-0.02049	-0.557
				$\vdots$	$\vdots$	$\vdots$

The introduction of the self-interaction correction leads to state-dependent effective potentials. Since all of them are very similar for all r, they have been replaced by a common average potential that is obtained as described in [27] (see also [28]). With this approximation, all the orbitals are now orthogonal since they are constructed from the same effective Hamiltonian. The energies of the occupied σ and π orbitals (respectively no nodes and one node in the radial wavefunction) in this average potential are given in Table 1. These energies are close due to the introduction of the SIC term, our values are slightly different from those reported in [22]. It can be seen that only σ orbitals with $l = 7, 8$ and 9 lie in the region of the π orbitals.

3.2 Ionization dynamics

The investigation on the ionization dynamics is carried out in the context of a recent experiment [9]. Under conditions where the pulse duration is shorter than 25 fs, ATI occurs in the absence of fragmentation. Furthermore, multiple ionization remains low for intensities below say 10^{14} W/cm^2. For these reasons, we restrict the present "frozen core and nucleus" approach to pulses lasting less than 25 fs with maximum intensities of 10^{14} W/cm^2. The photon energy is set to 1.57 eV ($\lambda = 790$ nm). During the interaction with the laser field, although we consider very

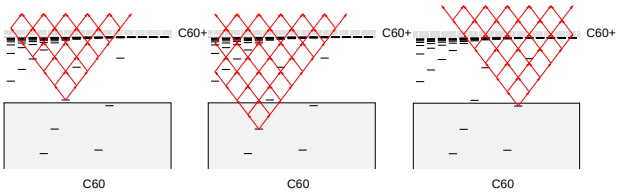

Fig. 8. Possible mechanisms considered in the ATI of C_{60}. 5-photon ionization from ($l = 5$, $n = 2$) left, 7-photon ionization from ($l = 4$, $n = 2$) center and 5-photon ionization from ($l = 9$, $n = 1$) right.

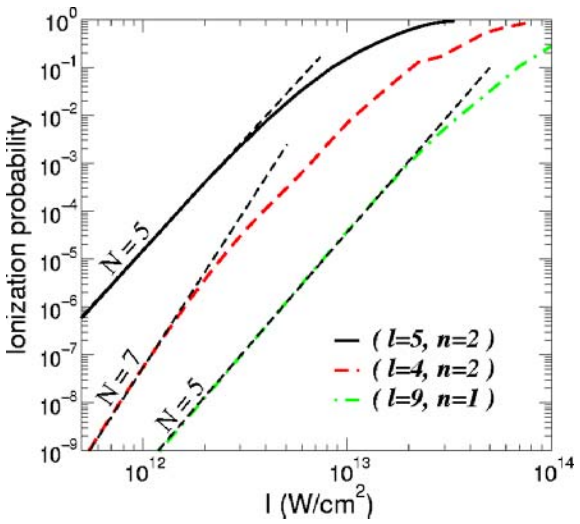

Fig. 9. Total ionization probability of C_{60} as a function of the peak intensity. Upper curve: initial state ($l = 5$, $n = 2$). Center curve: ($l = 4$, $n = 2$). Lower curve: ($l = 9$, $n = 1$). Thin dashed lines: perturbation theory with the corresponding slopes (process order N).

short durations, a significant heat is transfered to the electrons. The limit between occupied and unoccupied levels is therefore not so sharp anymore. As a matter of fact, our model implies the highest occupied level to be ($l = 9$, $n = 1$). However, the π state ($l = 5$, $n = 2$) is so close in energy that the quasi degeneracy can't be omitted. We thus have considered ionization from the few states that are the closest to the Fermi level. The possible ionization schemes are summarized in Figure 8.

We first have computed the total ionization of C_{60} for various laser field peak intensities by solving the TDSE as described briefly in the previous section: the Ar potential is changed to the cluster potential given in equation (9). The results are plotted in Figure 9. As expected, for low intensities, the ion yield (as a function of the intensity) is linear in a log-log plot thus depicting a perturbative behavior. We also have reported the ion yield computed within the lowest order perturbation theory (LOPT) to better identify the limit of the perturbative regime. The lower curve in Figure 9 gives the ionization of the cluster in the initial ($l = 9$, $n = 1$) state which occurs to be the HOMO in our model. The overall slope is clearly 5 if we consider intensities up to 2×10^{13} W/cm^2 as predicted by LOPT since it requires 5 photons to ionize the cluster from ($l = 9$, $n = 1$). This simple picture is limited however, because is involves the omission of other effects. Indeed, as the intensity raises, the ionization threshold ponderomotively shifts upward (by an energy of $U_p = I/4\omega^2$) eventually closing the 5-photon ionization channel and requiring at the same time the absorption of 6 photons to release the electron. Cranking up the intensity further will lead to successively open and close the 6-, 7-, 8-, ... photon ionization channels. In principle, according to LOPT, above intensities of 5.6×10^{12} W/cm^2 the ionization slope should be 6 before switching to 7 at $I = 3.2 \times 10^{13}$ and so on. In reality, the slope fluctuates but never exceed 5. This is due to the fact that slightly after the channel closures, the system becomes resonant with intermediate Rydberg states located somewhere below the ionization threshold. Some of these resonant states may get populated, creating Rabi oscillations and delaying the electron ejection. The multiphoton ionization process is no longer instantaneous and definitely breaks the I^N LOPT law. For higher intensities, the yield departs from a straight line because ionization starts to saturate. In the present case, saturation seems to happen around an intensity of 10^{14} W/cm^2.

The upper curve in Figure 9 corresponds to ionization from ($l = 5$, $n = 2$) which is energetically very close to the ($l = 9$, $n = 1$) state. The number of photons required to ionize is also 5 and perturbation theory works well up to $I = 3.0 \times 10^{12}$. However the probability is 4 orders of magnitude higher. Preliminary investigations show that this great difference is, at least, due to two reasons. By computing ionization cross-sections within LOPT, we have checked that the presence of the intermediate state ($l = 6$, $n = 2$) was responsible for a significant enhancement (just as in resonantly enhanced multiphoton ionization) although completely detuned from the one-photon absorption resonance (see the left graph in Fig. 8). Such an enhancement is absent in the case of ionization from ($l = 9$, $n = 1$). Note that this effect is only related to the unusual structure of the cluster where relatively low lying bound states play a major role in boosting the ionization. This is in contrast with the dynamics observed in rare gases where only high lying Rydberg states are involved. The other factor comes from the dipole couplings themselves. Their magnitude is in fact lower when starting from $l = 9$ than from $l = 5$. Because ionization involves at least 5 photons the accumulated difference can easily reach 2 or 3 orders of magnitude. The middle curve in Figure 9 gives the probability of ionizing from the inner shell ($l = 4$, $n = 2$). Although this process requires at least 7 photons its amplitude is still 2 orders of magnitude higher than ionization from ($l = 9$, $n = 1$).

3.3 Conclusion

We have performed non-perturbative calculations of ionization of C_{60} solving the TDSE where the cluster is represented by a model potential in the single active electron approximation. We have considered several initial states of C_{60} and concluded that even if our model defines ($l = 9$,

$n = 1$) as the ground state, ionization is more likely to occur from ($l = 5$, $n = 2$). The unavoidable temperature in the system broadens the Fermi level thus resulting in significant population in that state. A more sophisticated model potential is being developed that we hope will be able to reproduce the resonances observed recently [29].

One of the authors (E.C.) would like to acknowledge the support of the European Commission through grant number HPRI-CT-1999-00026 (the TRACS Program at EPCC) for high performance computing. Part of the calculations where also performed within the new M3PEC pole for parallel computing at University Bordeaux 1.

References

1. P. Agostini, F. Fabre, G. Mainfray, G. Petite, N.K. Rahman, Phys. Rev. Lett. **42**, 1127 (1979)
2. G.G. Paulus, W. Nicklich, Huale Xu, P. Lambropoulos, H. Walther, Phys. Rev. Lett. **72**, 285 (1994)
3. M.A. Walker, P. Hansch, L.D. van Woerkom, Phys. Rev. A **57**, R701 (1998)
4. D. Charalambidis, P. Lambropoulos, H. Schröder, O. Faucher, H. Xu, M. Wagner, C. Fotakis, Phys. Rev. A **50**, R2822 (1994)
5. C.J.G.J. Uiterwaal, D. Xenakis, D. Charalambidis, Z. Phys. D **38**, 309 (1996)
6. C.J.G.J. Uiterwaal, D. Xenakis, D. Charalambidis, P. Maragakis, H. Schröder, P. Lambropoulos, Phys. Rev. A **57**, 392 (1998)
7. B. Witzel, N.A. Papadogiannis, D. Charalambidis, Phys. Rev. Lett. **85**, 2268 (2000)
8. R. Lafon, J.L. Chaloupka, B. Sheehy, P.M. Paul, P. Agostini, K.C. Kulander, L.F. DiMauro, Phys. Rev. Lett. **86**, 2762 (2001)
9. E.E.B. Campbell, K. Hansen, K. Hoffmann, G. Korn, M. Tchaplyguine, M. Wittmann, I.V. Hertel, Phys. Rev. Lett. **84**, 2128 (2000)
10. H. Helm, N. Bjerre, M.J. Dyer, D.L. Huestis, M. Saeed, Phys. Rev. Lett. **70**, 3221 (1993)
11. C. Bordas, F. Pauling, H. Helm, D.L. Huestis, Rev. Sci. Instrum. **67**, 2257 (1996)
12. E. Cormier, P. Lambropoulos, J. Phys. B **30**, 77 (1997)
13. H. Bachau, E. Cormier, P. Decleva, J.E. Hansen, F. Martín, Rep. Prog. Phys. **64**, 1815 (2001)
14. H.G. Muller, F.C. Kooiman, Phys. Rev. Lett. **81**, 1207 (1998)
15. E. Cormier, D. Garzella, P. Breger, P. Agostini, G. Chériaux, C. Leblanc, J. Phys. B **34**, L9 (2001)
16. S. Augst, D.D. Meyerhofer, D. Strickland, S.L. Chin, J. Opt. Soc. Am. B **8**, 858 (1991)
17. V. Schyja, T. Lang, H. Helm, Phys. Rev. A **57**, 3692 (1998)
18. R.R. Freeman, Bucksbaum, H. Milchberg, S. Darack, D. Scumacher, M.E. Geusic, Phys. Rev. Lett. **59**, 1092 (1987)
19. P. Agostini, P. Breger, A. L'huillier, H.G. Mueller, G. Petite, Phys. Rev. Lett. **63**, 2208 (1989)
20. H. Helm, M.J. Dyer, Phys. Rev. A **49**, 2726 (1994)
21. R. Wiehle, B. Witzel, Phys. Rev. Lett. **89**, 223002 (2002)
22. M.J. Puska, R.M. Nieminen, Phys. Rev. A **47**, 1181 (1993)
23. O. Gunnarsson, B.I. Lundqvist, Phys. Rev. B **13**, 4274 (1976)
24. J.P. Perdew, A. Zunger, Phys. Rev. B **237**, 5048 (1981)
25. V.K. Ivanov, G.Yu. Kashenock, R.G. Polozkov, A.V. Solov'yov, J. Phys. B **34**, L669 (2001)
26. I.V. Hertel, Phys. Rev. Lett. **68**, 784 (1992)
27. M.F. Politis, P.A. Hervieux, J. Hanssen, M.E. Madjet, F. Martín, Phys. Rev. A **58**, 367 (1998)
28. C.A. Ullrich, P.G. Reinhard, E. Suraud, Phys. Rev. A **62**, 053202 (2000)
29. M. Boyle, K. Hoffmann, C.P. Schulz, I.V. Hertel, R.D. Levine, E.E.B. Campbell, Phys. Rev. Lett. **87**, 273401 (2001)